Nanoscale Advances

ROYAL SOCIETY OF CHEMISTRY

PAPER

View Article Online
View Journal | View Issue

Cite this: *Nanoscale Adv.*, 2026, **8**, 3256

Synthesis of azole-linked *s*-triazine-isatin molecular architectures as nanoscale DNA-targeting agents: a combined spectroscopic and computational study

Alia Mushtaq, Bibi Nazia and Muhammad Moazzam Naseer *

DNA, a ~2 nm diameter biopolymer, represents a fundamental nanoscale target for anticancer therapeutics due to its central role in replication and transcription. In parallel, DNA topoisomerase II (topo II), a key regulator of DNA topology, remains a validated enzymatic target for chemotherapeutic intervention. Herein, we report the synthesis of a series of azole-linked *s*-triazine-isatin hybrids **9a–f** designed as multifunctional nanoscale DNA-targeting architectures. The nano-bio interactions of these hybrids with salmon sperm DNA (SS-DNA) were systematically investigated under physiological conditions (pH 7.4) using UV-vis absorption spectroscopy. Binding constants (K_b), determined using Benesi–Hildebrand analyses, ranged from 10^3 to 10^5 M^{-1}, with **9f** showing the highest affinity (1.20×10^5 M^{-1} at 298 K), comparable to the reference standard. The Gibbs free energy change ($\Delta G = -28.9$ kJ mol^{-1}) indicated that the binding of **9f** is spontaneous. Molecular docking studies supported these experimental findings, revealing that **9f** forms stabilizing hydrophobic and hydrogen-bonding interactions within AT-rich DNA grooves (docking score: −10.3 kcal mol^{-1}, PDB: 3EY0) and binds topoisomerase II with a docking score of −10.7 kcal mol^{-1} (PDB: 3QX3). Molecular dynamics simulations further confirmed the structural stability and dynamic behavior of the DNA–ligand and protein–ligand complexes. In addition, DFT calculations and *in silico* drug-likeness evaluations provided insights into electronic properties and pharmacokinetic potential. Collectively, these results highlight azole-linked *s*-triazine-isatin hybrids as promising nanoscale DNA-targeting scaffolds for anticancer development.

Received 17th December 2025
Accepted 25th April 2026

DOI: 10.1039/d5na01140j

rsc.li/nanoscale-advances

1. Introduction

Cancer continues to be a major global health challenge, representing a leading cause of morbidity and mortality worldwide and highlighting the urgent need for effective and selective therapeutics.[1–5] Among molecular targets, DNA occupies a central position in anticancer drug development, as small molecules capable of binding DNA can disrupt replication, transcription, and other essential cellular processes, ultimately leading to cytotoxic effects.[3,6–11] Structurally, DNA is a nanoscale biopolymer approximately 2 nm in diameter, characterized by sequence-dependent grooves and electrostatic surface features that enable selective molecular recognition.[12,13] Ligand–DNA interactions represent nanoscale supramolecular recognition processes governed by noncovalent forces such as π–π stacking, hydrogen bonding, electrostatic contacts, and van der Waals interactions.[14–18] These interactions may occur through groove binding, intercalation, or external association, with binding affinity and specificity strongly influenced by ligand topology and electronic structure.

In addition to direct DNA targeting, DNA topoisomerase II (topo II) plays a critical role in regulating DNA topology during replication and transcription.[19] Clinically used topo II-targeting agents such as etoposide and doxorubicin stabilize the topo II–DNA cleavage complex, leading to DNA damage and apoptosis.[20] However, their therapeutic utility is limited by resistance and systemic toxicity, motivating the exploration of new molecular scaffolds capable of interacting with DNA and potentially modulating topo II activity.[21]

Heterocyclic pharmacophores such as *s*-triazine and isatin are well-established motifs in medicinal chemistry, exhibiting diverse biological activities including anticancer and DNA-interactive properties.[22–32] Triazine cores are present in approved drugs such as altretamine and gedatolisib, while isatin derivatives—including sunitinib and nintedanib—demonstrate enzyme inhibition and nucleic acid interactions.[33–40] Azole-containing heterocycles (*e.g.*, benzothiazoles, benzoxazoles, tetrazoles) are electron-rich aromatic systems capable of forming hydrogen bonds and π–π stacking interactions, making them attractive candidates for DNA recognition.[41–50]

Pharmacophore hybridization, which integrates complementary structural motifs into a single molecular framework,

Department of Chemistry, Quaid-i-Azam University, Islamabad 45320, Pakistan. E-mail: moazzam@qau.edu.pk

has emerged as a rational strategy to enhance biological activity and binding affinity.[51–55] Inspired by this approach and our previous investigations on *s*-triazine and isatin derivatives,[56–59] we designed and synthesized a series of azole-linked *s*-triazine-isatin hybrids **9a–f**. Their DNA-binding interactions were evaluated using UV-Vis absorption spectroscopy with SS-DNA. To further elucidate nanoscale recognition features and interaction stability, molecular docking, molecular dynamics simulations, density functional theory (DFT) calculations, and *in silico* ADMET analyses were performed. Collectively, this integrated experimental–computational study aims to characterize the DNA-recognition properties of these hybrid heterocycles and to provide a structural foundation for the future development of DNA-interactive scaffolds.

2. Results and discussion

2.1 Chemistry

For the synthesis of azole linked *s*-triazine-isatin hybrids **8a–f** (Scheme 1), cyanuric chloride **1** was reacted with **2** equivalents of various substituted phenols using anhydrous potassium carbonate as an acid scavenger for liberated hydrochloric acid.[60] The reaction was initiated at ice-cold temperatures and subsequently transitioned to room temperature to minimize the formation of tri-substituted side products. The diphenoxy-linked *s*-triazines **2** were subsequently reacted with hydrazine monohydrate at room temperature,[61] yielding *s*-triazine-based hydrazines **3** (Scheme 1).

Similarly, the synthesis of intermediate **5** was achieved by reacting isatin **4** with dibromoethane (4 eq) in DMF at 50 °C, using K_2CO_3 as a base to neutralize the generated HCl (Scheme 1). The resulting 1-(2-bromoethyl)isatin **5** were then reacted with respective azoles **6a–d** using K_2CO_3 in dimethylformamide (DMF) at 70–80 °C, affording the azole-pendant isatins **7a–d** in good yields.[62,63] In the final step, intermediate **5** and azole-pendant isatins **7a–d** were independently reacted with *s*-triazine-based hydrazines **3** refluxed in the presence of ethanol and a few drops of glacial acetic acid to afford a series of *s*-triazine-isatin hybrid **8** and amide linked *s*-triazine-isatin-hybrids **9a–f** (Scheme 1).

The chemical structures of the newly synthesized compounds **8** & **9a–f** were elucidated through comprehensive characterization using spectroscopic techniques, including FTIR, NMR, and MS analyses. In the ^{1}H NMR spectrum of compound **8**, the hallmark singlet for –NH protons of hydrazone moiety appeared at 12.86 ppm. Moreover, the absence of –NH_2 protons of compound **3** also evidenced the hydrazone formation by the condensation of *s*-triazine-based hydrazines with the carbonyl of isatin. The aromatic region is characterized by multiplets corresponding to 12-proton integration within the δ 6.92–7.68 range, validating the substitution pattern on the aromatic rings. The appearance of two triplets at 4.19 ppm and 3.74 ppm integrating two protons each, was assigned to ethylene linkage (–CH_2–CH_2–). Moreover, in the ^{13}C NMR spectra of compound **8**, the absence of keto-carbonyl carbon further supported the formation of hydrazones. The signal in the aliphatic region at 41.2 and 29.8 suggested the presence of ethylene linkage (–CH_2–CH_2–). Additionally, the signals observed in the range of 118.7 to 161.5 were attributed to the aromatic carbons of the targeted *s*-triazine-isatin hybrid **8** (see experimental section for further details).

Likewise, in the ^{1}H NMR and ^{13}C NMR spectrums of azole linked *s*-triazine-isatin hybrids **9a–f**, additional proton count and carbon signals in aromatic region respectively suggest the

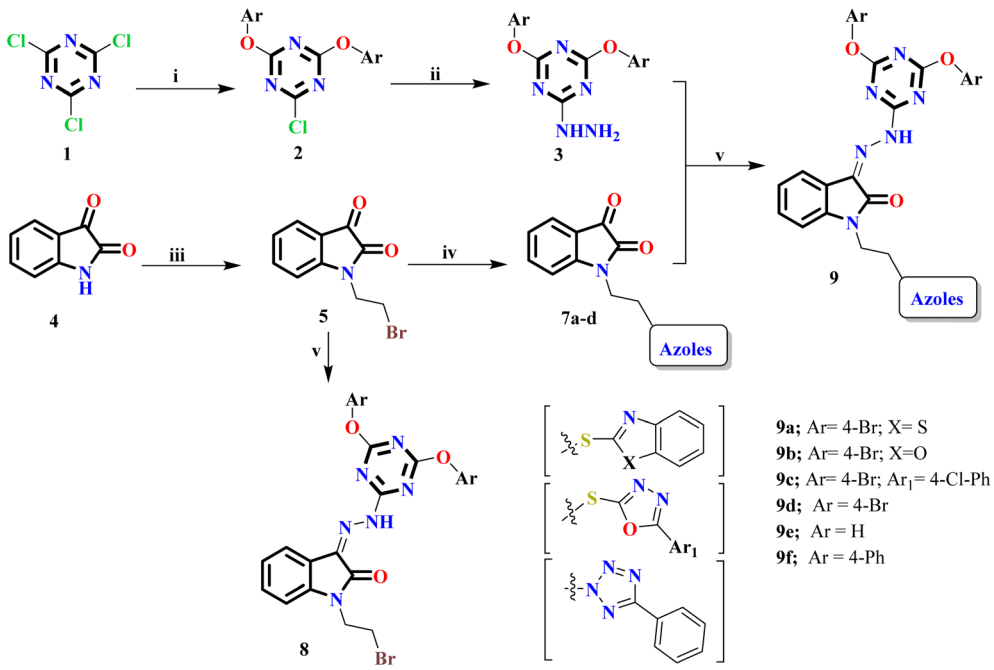

Scheme 1 Synthetic pathway of azole linked *s*-triazine-isatin hybrids **9a–f**.

presence of respective azole moiety. The ^{1}H NMR spectrum of a representative compound **9e** confirmed the key structural features of the synthesized compound. Two triplets observed at δ 4.38 and δ 5.02, each having two proton integration were assigned to methylene protons, supporting the presence of an ethylene linker between the isatin and tetrazole moieties. A distinct downfield singlet at δ 12.74 was attributed to the NH proton, characteristic of hydrazone functionality. In the aromatic region (δ 6.60–8.03), multiplets integrating for a total of 19 protons were recorded, consistent with multiple phenyl substituents and in full agreement with the proposed molecular structure.

Additionally, the ^{13}C NMR spectrum further confirmed the proposed structure of compound **9e**. Signals at δ 39.3 and δ 50.1 in the aliphatic region were assigned to methylene carbons, confirming the presence of the ethylene linker. A distinct resonance at δ 135.0 corresponded to the imine carbon, providing evidence for the formation of the hydrazone linkage. The peak at δ 161.0 was attributed to the tetrazole carbon and lactam carbonyl, while the most downfield signals at δ 165.7 and δ 167.2 were characteristic of *s*-triazine carbons, thereby confirming the incorporation of the triazine core. The remaining signals in the aromatic region were fully consistent with the expected aromatic carbons. Furthermore, the FTIR spectral analysis revealed distinct absorption bands characteristic of the functional groups supporting the structural frameworks of the synthesized comouunds (See experimental section for further details).

2.2 DNA binding studies

The DNA-binding affinity of the synthesized *s*-triazine-isatin hybrids **8** & **9a–f** was evaluated through UV-vis spectroscopic titrations, and the corresponding binding constants (K_b) and binding free energies (ΔG) were calculated to quantify their interaction with SS-DNA. The results are summarized in Table 1. All compounds exhibited varying degrees of SS-DNA interaction, with distinct structure–activity relationships that reflect the influence of both azole substitution and the R_1 group on binding behavior.

Among the evaluated compounds, **9f** (R_1 = 4-Ph, azole = tetrazole) showed the highest binding affinity, with a K_b value of 1.20×10^5 M^{-1} (Table 1) which was associated with the most favorable binding free energy ($\Delta G = -28.9$ kJ mol^{-1} for both),

Table 1 Results of the determination of the binding constants (K_b) at room temperature and binding free energies (ΔG) of compounds (**9a–f**)-DNA complex

Compounds	R_1, azole	K_b (M^{-1})	ΔG (kJmol^{-1})
8	4-Br, _	$4.63 \times 10^3 \pm 0.85$	-20.9 ± 0.83
9a	4-Br, benzothiazole	$4.24 \times 10^4 \pm 0.31$	-26.4 ± 0.61
9b	4-Br, benzoxazole	$3.34\times 10^3 \pm 0.13$	-20.1 ± 0.24
9c	4-Br, oxadiazole	$1.16 \times 10^5 \pm 0.10$	-28.9 ± 0.94
9d	4-Br, tetrazole	$9.70 \times 10^3 \pm 0.23$	-22.7 ± 0.35
9e	H, tetrazole	$3.92 \times 10^4 \pm 0.27$	-26.2 ± 0.55
9f	4-Ph, tetrazole	$1.20 \times 10^5 \pm 0.04$	-28.9 ± 0.03
CBZ	—	5.79×10^5 [10]	-32.8[10]

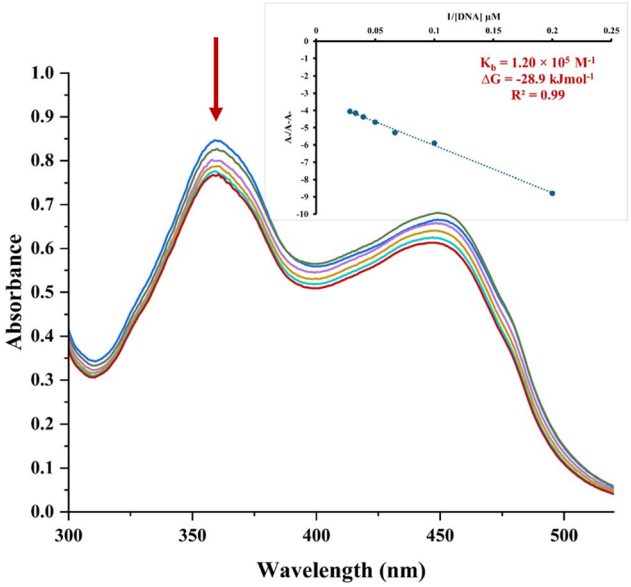

Fig. 1 UV-vis absorption spectrum of compound **9f** at pH 7.4 and room temperature, with and without varying SS-DNA concentrations (5–35 μM), demonstrating spectral shifts indicative of groove binding interactions. Inset: plot of $A_o/(A-A_o)$ as a function of 1/[DNA].

indicating thermodynamically stable and spontaneous interactions (Table 1). The enhanced SS-DNA affinity of **9f** can be attributed to multiple nitrogen atoms capable of forming hydrogen bonds, while the 4-phenyl substituent likely facilitates additional π–π stacking interactions with nucleobase pairs, contributing to overall binding stabilization and displayed hypochromic shift without showing a bathochromic shift (Fig. 1), indicative of SS-DNA groove binding.

Similarly, compound **9c** ($R1$ = 4-Br, azole = oxadiazole) exhibited the highest binding affinity, with a K_b value of 1.16×10^5 M^{-1} (Table 1) suggesting thermodynamically stable and spontaneous interactions. The superior SS-DNA affinity of **9c** is likely due to the electron-rich, planar nature of the oxadiazole moiety, which facilitates π–π stacking and potential hydrogen-bonding interactions within the SS-DNA helix.

Compounds **9a** and **9e** also exhibited substantial binding affinities, with K_b values of 4.24×10^4 M^{-1} and 3.92×10^4 M^{-1}, and ΔG values of -26.4 and -26.2 kJ mol^{-1}, respectively (Table 1). The benzothiazole ring in **9a** may interact with SS-DNA through sulfur-mediated interactions or hydrophobic contacts, while the high affinity of **9e**, despite lacking an R_1 substituent, suggests that the tetrazole moiety dominantly governs its interaction mode.

Conversely, compounds **8** and **9b** exhibited weaker SS-DNA binding, as evidenced by their lower binding constants (4.63×10^3 M^{-1}and 3.34×10^3 M^{-1} respectively; Fig. S1) and less negative free energy changes (-20.9 and -20.1 kJ mol^{-1} respectively). The reduced binding affinity of **9b** may be attributed to the benzoxazole moiety, which likely provides suboptimal electronic and steric complementarity for effective interaction with SS-DNA. In the case of compound **8**, the absence of an extended heteroaromatic system may limit π–π

stacking and hydrogen-bonding interactions with the SS-DNA structure.

Spectroscopic analysis of *s*-triazine-isatin hybrids **8** & **9a–f** further supported these findings (Fig. S1). All the compounds exhibited hypochromism upon SS-DNA addition, indicative of strong π–π stacking or groove binding interactions between the conjugated systems and SS-DNA base pairs. Notably, compounds **9a–9c** showed hypochromism accompanied by slight bathochromic shifts (red shifts), suggesting partial intercalation and significant stabilization of the excited state upon SS-DNA binding. In contrast, **8**, **9d**, and **9e** demonstrated hypochromism with slight hypsochromic shifts (blue shifts) (Fig. S1), implying a non-intercalative binding mode, such as minor groove binding, possibly due to a more polar or constrained environment around the chromophore upon complexation. Interestingly, compound **9f**, which exhibited the strongest overall binding affinity, comparable to standard cabozantinib (CBZ), showed notable hypochromism without any significant shift (Fig. 1), indicating a groove binding mode of interaction.

These spectral features, taken together with the calculated thermodynamic parameters, highlight the critical role of azole ring structure and R_1 substitution in determining not only the binding strength but also the interaction mode with DNA. Electron-rich, planar heterocycles such as oxadiazole and tetrazole significantly enhance binding through a combination of π–π stacking, hydrogen bonding, and groove-directed interactions, thereby offering valuable design elements for the development of DNA-targeted small molecules.

Compared to classical groove binders such as netropsin and Hoechst dyes, which exhibit binding constants in the range of (10^3–10^5 M^{-1}),[64,65] the synthesized compounds fall within a comparable regime, supporting their classification as moderate-affinity groove-binding ligands. For instance, azole- and isatin-based DNA binders typically exhibit binding constants in the range of 10^4–10^6 M^{-1},[66] depending on molecular planarity and electronic characteristics. In contrast, classical intercalators generally display significantly higher binding affinities (>10^6 M^{-1}) due to strong π–π stacking interactions with DNA base pairs.[65,67] Therefore, the moderate binding affinities observed for compounds **9a–9f** support a groove-binding mode rather than intercalation. Overall, these results are in good agreement with reported drug–DNA interaction studies, where structurally balanced heterocyclic systems preferentially bind within the DNA groove without inducing significant helical distortion.

2.3 Molecular docking analyses

To rationalize the DNA-binding affinity of the synthesized compounds **8** & **9a–f**, molecular docking simulations were performed against the DNA double-helix DNA sequence: 5′-(ATATATATAT)-3′, (PDB ID: 3EY0) and key interactions were analyzed (Table 2). All compounds exhibited favorable binding energies, engaging in a variety of non-covalent contacts, predominantly with adenine and thymine bases across both DNA strands. The docking studies revealed that the compounds preferentially bind within the groove of the AT-rich regions, forming multiple stabilizing hydrogen bonds and hydrophobic contacts (Fig. 2).

The parent compound **8**, bearing a 4-bromophenyl moiety, exhibited a docking score of −8.0 kcal mol^{-1} (Table 2). The interaction network was characterized by hydrogen bonding with DA5 (A) and DA7 (B), along with π–anion interaction with DT2 (A), π–π T-shaped stacking with DT4 (A) and DA3 (A), π–donor

Table 2 Estimated docking scores and interaction profiles of compounds **8** & **9a–f** with DNA (3EY0)

			Compound-DNA interactions	
Compounds	R_1, azole	Docking score	Hydrogen bonding	Hydrophobic
8	4-Br	−8.0	DA5 (A), DA7 (B)	DT2 (A) Pi-anion; DT4 (A), DA3 (A) Pi–Pi T shaped; DT6 (B), DA5 (B) Pi-donor hydrogen bond; DT4 (B) van der Waals
9a	4-Br, benzothiazole	−8.2	DA5 (A), DT4 (A), DA7 (B), DT4 (B)	DT2 (A)Pi-anion; DT6 (B), DA3 (A) Pi–Pi T shaped, Pi–Pi stacked; DA5 (B) Pi-donor hydrogen bond, van der Waals
9b	4-Br, benzoxazole	−8.1	DA5 (A), DA5 (B), DT6 (B), DA7 (B)	DA3 (A), DT4 (A) Pi–Pi T shaped, Pi–Pi stacked; DT2 (A) Pi-anion; DT4 (B)Pi-donor hydrogen bond, Pi-alkyl, van der Waals
9c	4-Br, oxadiazole	−9.4	DA5 (A), DA7 (B)	DT6 (B), DA3 (A), DT4 (A), DT2 (B) Pi–Pi T shaped, Pi–Pi stacked; DT4 (B) Pi-sigma; DA3 (B), DA5 (B) Pi-donor hydrogen bond, DT6 (A), DA7 (A), van der Waals; DT2 (A) Pi-anion
9d	4-Br, tetrazole	−11.1	DA5 (A), DA5 (B), DT6 (A)	DA9 (A), DA9 (B), DT10 (A), DT4 (B), DT6 (B) van der Waals; DT8 (A), DA7 (B) Pi-anion; DA7 (A) Pi–Pi stacked; DT8 (B) carbon hydrogen bond
9e	H, tetrazole	−11.4	DA5 (A), DA5 (B), DA7 (A)	DT8 (B) Pi-anion; DT6 (B), DT8 (A) carbon hydrogen bond; DA9 (A), DA7 (B), DT6(A), DA9 (B), DT4 (A) van der Waals
9f	4-Ph, tetrazole	−11.5	DA5 (A), DA5 (B), DT6 (B), DA7 (A)	DA9 (A), DT8 (B), Pi-anion; DT4 (B), DA9 (B), DT4 (A), DT6(A), DA7 (B) van der Waals; DT8 (A) carbon hydrogen bond

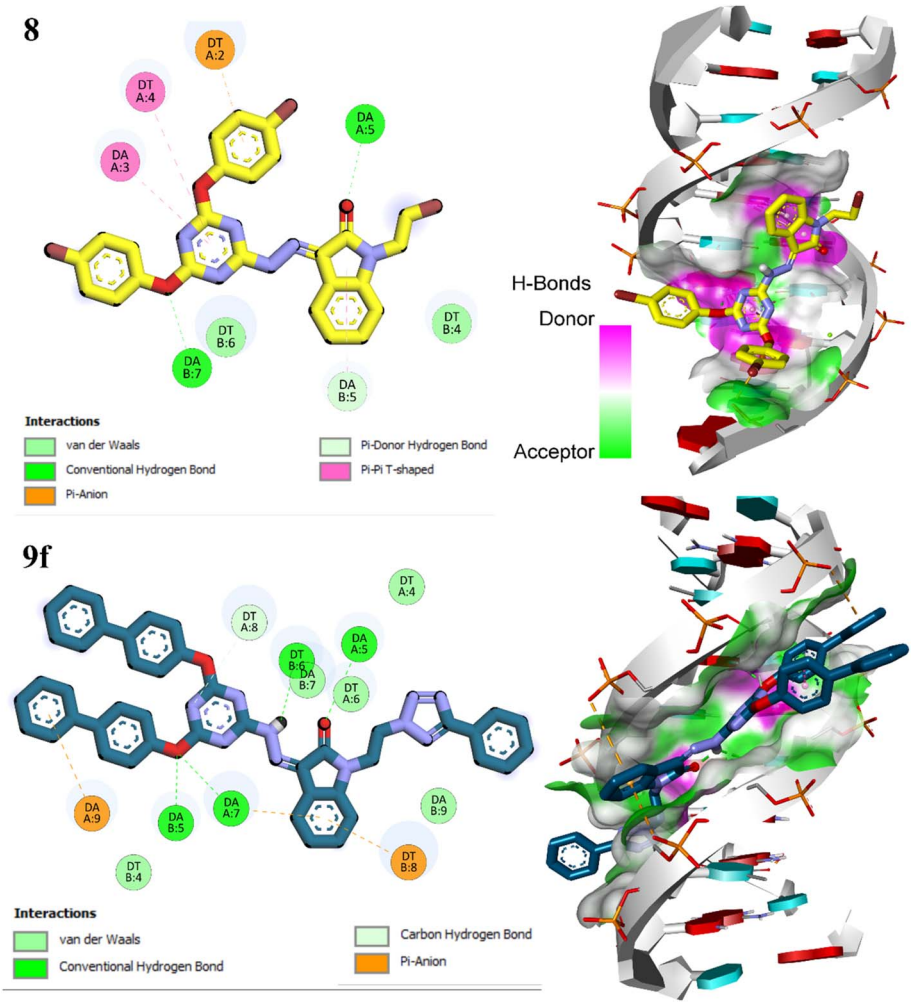

Fig. 2 2D and 3D binding poses of weak binder **9b** (yellow)and strong binder **9f** (blue) with DNA (PDB ID: 3EY0), illustrating major and minor groove binding interactions respectively.

hydrogen bonding with DT6 (B) and DA5 (B) and van der Waals contacts with DT4 (B). The modest binding energy reflects limited heteroaromatic surface area and interaction versatility.

In contrast, the incorporation of azole heterocycles in **9a–f** markedly enhanced DNA affinity and interaction complexity. Compounds **9a** (benzothiazole) and **9b** (benzoxazole) showed improved docking scores of −8.2 and −8.1 kcal mol^{-1}, respectively, with extended hydrogen-bonding networks (*e.g.*, DA5, DT4, DA7) and multiple π–π stacking and π–anion interactions (Table 2). These interactions were facilitated by the planar aromatic heterocycles, enabling favorable π-surface complementarity within the DNA minor groove (Fig. S2). Significantly, compound **9c**, featuring an oxadiazole motif, achieved a docking score of −9.4 kcal mol^{-1}. It formed strong π–π stacking (DT6, DA3), π–donor hydrogen bonds (DA3, DA5), and van der Waals contacts, suggesting improved electrostatic and shape complementarity. The increased heteroatom density in oxadiazole may also enhance hydrogen bond acceptor potential.

The tetrazole-bearing analogs **9d–f** demonstrated the highest docking affinities (−11.1 to −11.5 kcal mol^{-1}) (Table 2) with the binding in minor groove of DNA (Fig. 2). Compound **9d** (4-Br, tetrazole) formed key hydrogen bonds with DA5 and DT6, π–anion interactions with DT8, and π–π stacking with DA7. Notably, compound **9e**, lacking a halogen but retaining the tetrazole, showed comparable binding (−11.4 kcal mol^{-1}), indicating the dominant role of the tetrazole in anchoring the ligand. The highest scoring compound, **9f** (4-phenyl, tetrazole), engaged in a dense interaction network, including hydrogen bonding (DA5, DA7), π–anion (DA9, DT8), and extensive van der Waals interactions, underscoring the beneficial impact of increased aromatic surface area and substitution bulk (Fig. 2). Moreover, a qualitative correlation between experimental binding constants and docking scores was observed. Compounds **9c** and **9f**, which exhibited the highest K_b values ($\approx 10^5$ M^{-1}), also showed the most favorable docking scores (−9.4 to −11.5 kcal mol^{-1}), supporting consistency between spectroscopic and computational findings.

Furthermore, comparative docking analysis revealed distinct binding modes for compounds **8** and **9f** with DNA (PDB ID: 3EY0). Compound **8** binds weakly within the major groove, forming few and low-strength non-covalent interactions, which resulted in limited complex stabilization (Fig. 2). In contrast,

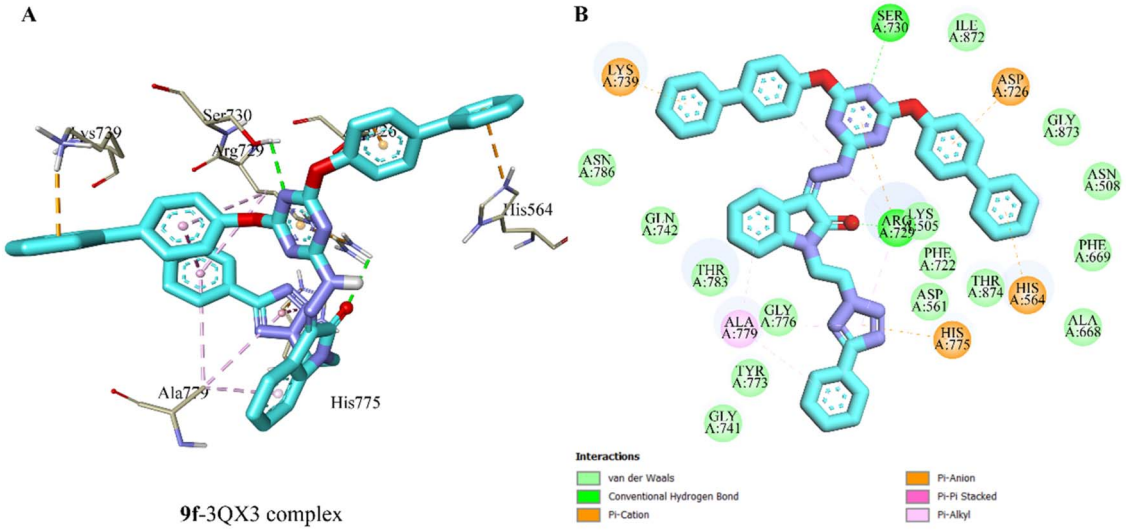

Fig. 3 Molecular docking of compound **9f** (cyan) with topoisomerase II (3QX3). (A) 3D binding conformation within the active site, indicating key residue interactions. (B) 2D interaction map illustrating hydrogen bonds and hydrophobic contacts contributing to binding stability.

compound **9f** preferentially occupied the minor groove, where it established multiple hydrogen bonds and hydrophobic contacts, leading to enhanced binding stability. The superior affinity of **9f** is attributed to its better geometric complementarity and higher interaction density within the confined minor groove environment compared to compound **8.**

Collectively, the docking data underscore the critical influence of the azole pharmacophore on DNA-binding affinity. Among these, the tetrazole scaffold consistently enabled deeper DNA groove accommodation and maximized stabilizing interactions, supporting its potential as a privileged motif for the design of DNA-targeted drug development.

Moreover, molecular docking analyses of top scorer compound **9f** was also performed with topoisomerase II (PDB: 3QX3). Docking analyses indicated that active site residues such as ARG729, SER 730, GLN742, TYR773, HIS775, and ASN 786 a crucial role in interacting ligands with the binding pocket of protein. Findings showed that compound **9f** undergo several hydrogen bond interactions besides van der Waals, pi-cation, pi-anion, pi–pi stacked and pi-stacked interactions within the active site of topoisomerase II enzyme (A-chain) (Fig. 3). Interestingly, the docking score of compound **9f** (-10.7 kcal mol^{-1}) was found higher than the cocrystallized ligand etoposide (-9.5 kcal mol^{-1}).

2.4 MD simulation analyses

Compound **9f** was selected for MD simulation based on its highest experimental binding constant, most favorable docking score, and optimal aromatic surface complementarity within the DNA minor groove. The DNA-**9f** complex was prepared using the Amber ff19SB force field for DNA and GAFF2 parameters for the ligand. The system was solvated with the TIP3P water model, neutralized with sodium and chloride ions to mimic physiological conditions, and subjected to energy minimization followed by NVT and NPT equilibration. A 4 ns production simulation was then performed to generate trajectories for analysis.[68]

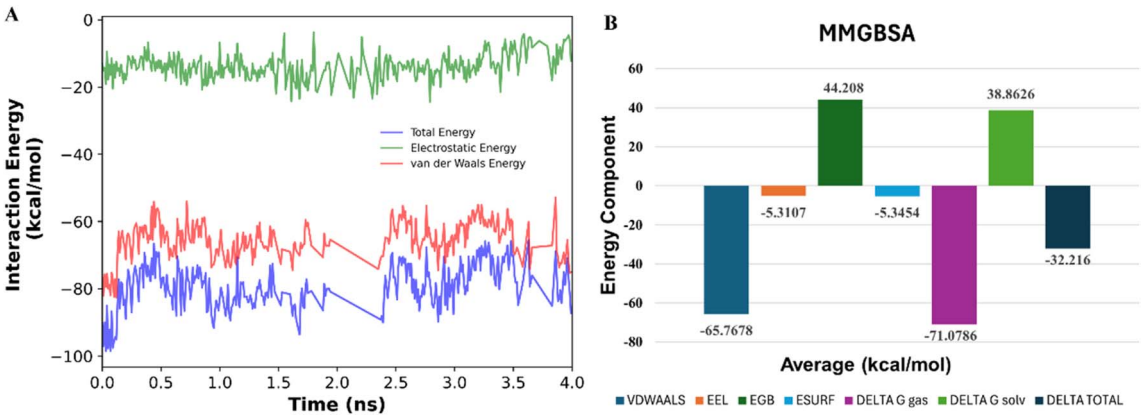

Fig. 4 MM/GBSA-derived binding free energy profile of compound **9f**: (A) fluctuation of total, electrostatic, and van der Waals interaction energies throughout the simulation trajectory, (B) contribution of individual energy terms to the overall binding free energy, highlighting the dominant stabilising interactions (kcal mol^{-1}).

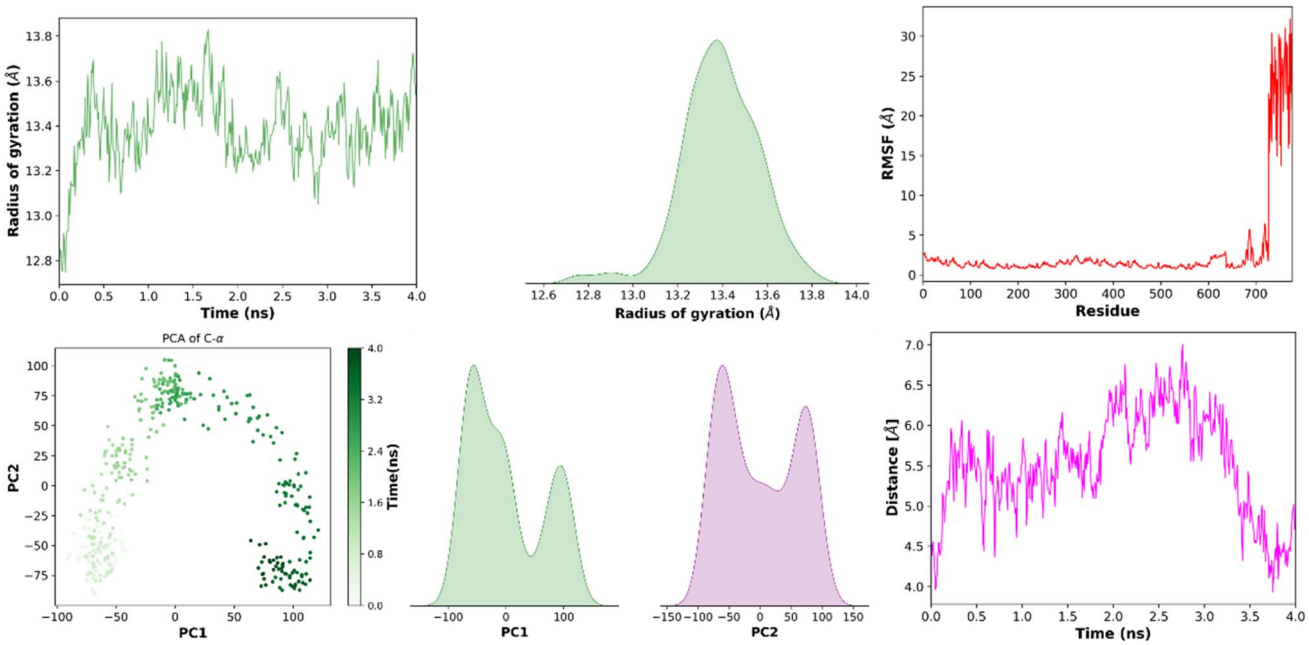

Fig. 5 Integrated MD simulation analyses of the DNA–9f complex.

MM/GBSA binding energy decomposition (Fig. 4) revealed that van der Waals interactions are the primary stabilizing force governing complex formation, while electrostatic and nonpolar solvation contributions further support binding. As expected in aqueous systems, polar solvation opposes binding due to desolvation penalties. The overall binding free energy ($\Delta G \approx -32$ kcal mol^{-1}) indicates thermodynamically favorable minor–groove association. Structural stability analyses further supported this observation. The radius of gyration remained stable at ~13.4 Å, indicating preservation of duplex integrity without unfolding (Fig. 5). RMSF analysis showed that flexibility was mainly confined to terminal nucleotides, whereas residues within the minor groove exhibited reduced fluctuations, consistent with localized backbone stabilization. Principal component analysis (PCA) demonstrated that PC1 and PC2 account for 72% of total motion, with the complex sampling a restricted conformational space relative to free DNA. The ligand–DNA distance remained stable throughout the trajectory, supporting persistent groove accommodation. Overall, the simulations indicate that **9f** occupies the ~6–8 Å minor groove without inducing global helix distortion, highlighting nanoscale geometric and electrostatic complementarity.

To evaluate potential protein interactions, MD simulations were also conducted for the **9f**–topoisomerase II complex (PDB ID: 3QX3) using GROMACS 2021.5 with the AMBER99SB force field. The system was solvated in a cubic box with TIP3P water and neutralized with counterions, followed by energy minimization and two-stage equilibration (NVT at 300 K and NPT at 1 bar). A 10 ns production run was performed under periodic boundary conditions using PME electrostatics and a 1.0 nm cutoff for nonbonded interactions.

The protein–ligand complex exhibited stable dynamics throughout the simulation. Backbone RMSD stabilized after ~2 ns and fluctuated around an average of ~3.0 Å (Fig. 6A), indicating equilibration and structural consistency. The radius of gyration (3.35 ± 0.05 nm) and solvent-accessible surface area (360 ± 10 nm^2) remained stable (Fig. 6B and C), confirming preservation of overall protein compactness. RMSF analysis showed that loop regions displayed higher mobility (0.25–0.80 nm), whereas residues within the binding pocket exhibited reduced fluctuations in the presence of the ligand (Fig. S3A), indicating localized stabilization. Hydrogen-bond analysis identified 2–3 persistent intermolecular hydrogen bonds with occupancies exceeding 80% (Fig. S3B), supporting stable interaction.

Energy decomposition analysis demonstrated that van der Waals interactions (−131.9 ± 8.3 kJ mol^{-1}) dominate complex stabilization, with electrostatic interactions providing additional favorable contributions. MM-PBSA calculations yielded a negative binding free energy (ΔG_binding = −4.76 ± 0.81 kcal mol^{-1}), confirming thermodynamic feasibility. PCA revealed that ligand binding restricts large-scale protein motions, with PC1 and PC2 capturing 72% of the variance (Fig. S4). The free energy landscape (Fig. S5) further showed that the ligand–bound complex occupies a deeper and more confined minimum compared to the apo state, indicating a shift toward energetically stabilized conformations.

Collectively, these MD simulations demonstrated that compound **9f** formed dynamically stable complexes with both DNA and topoisomerase II, primarily stabilized by hydrophobic and dispersive interactions. The convergence of spectroscopic data, docking results, and dynamic analyses supported a non-covalent, groove-directed DNA binding mode and highlighted the role of aromatic surface topology and electronic balance in governing nanoscale biomolecular recognition.

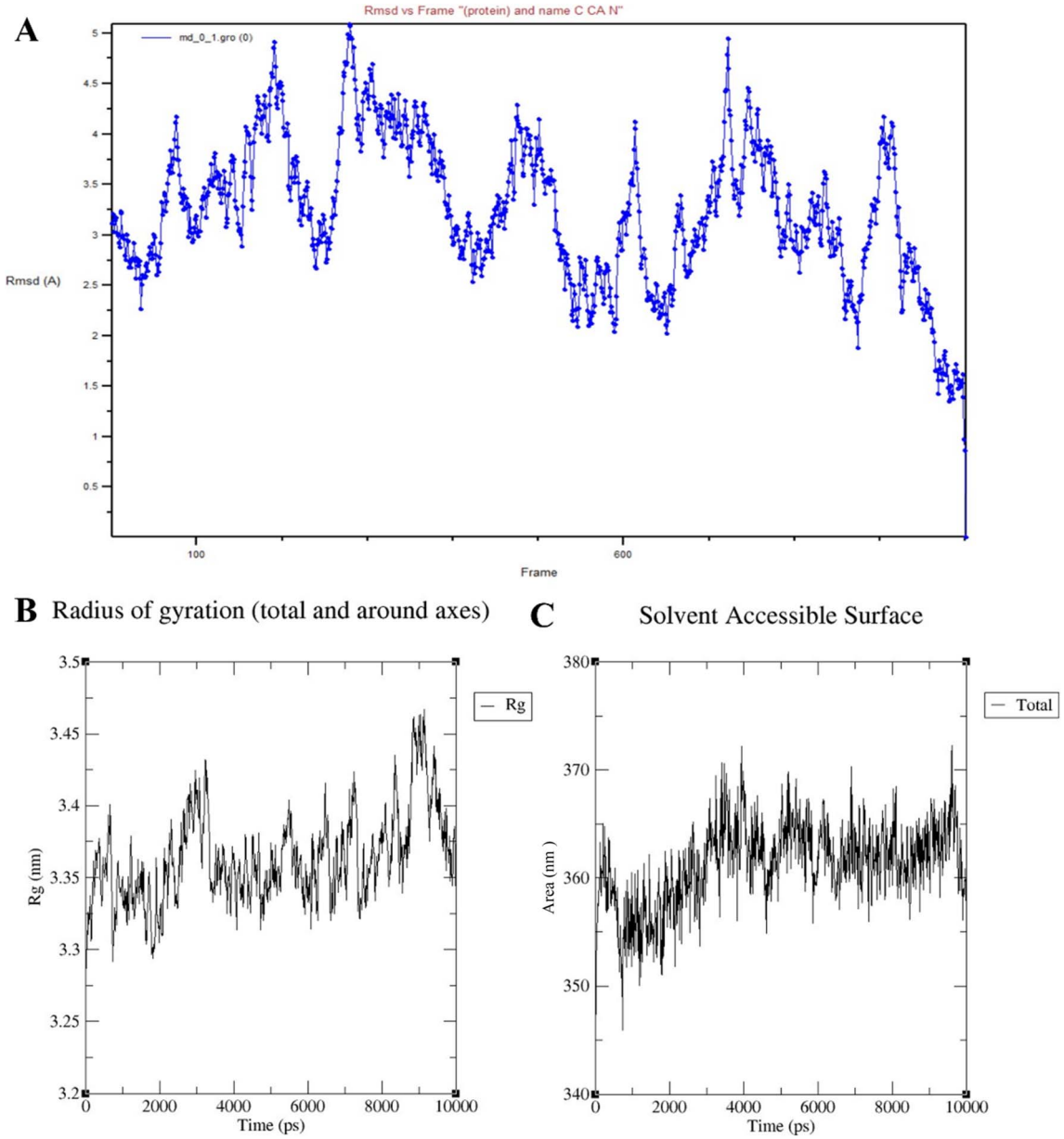

Fig. 6 Structural stability of protein–UNK complex. (A) Backbone RMSD over time (B) radius of gyration (C) solvent-accessible surface area.

2.5 DFT studies

To gain insight into the electronic properties and chemical reactivity of the synthesized compounds, DFT calculations were carried out for the parent *s*-triazine-isatin hybrid **8** and a series of azole-linked *s*-triazine-isatin hybrids **9a–f**. The calculated parameters include frontier molecular orbital energies (E_{HOMO}, E_{LUMO}), energy gap (ΔE_{gap}), ionization potential (IP), electron affinity (E_A), electronegativity (χ), electrochemical potential (μ), chemical hardness (η), softness (S), and electrophilicity index (ω), as summarized in Table 3.

Compound **9f**, bearing a 4-phenyl-substituted tetrazole moiety, exhibited electronic characteristics that distinguish it within the series and may rationalize its comparatively stronger DNA-binding behavior. The calculated HOMO (−6.10 eV) and LUMO (−2.44 eV) energies afforded a moderate energy gap (ΔE_{gap} = 3.65 eV), indicating a balanced combination of thermodynamic stability and electronic adaptability. This intermediate band gap suggested that **9f** is sufficiently reactive to participate in noncovalent biomolecular interactions while maintaining structural stability. Its ionization potential (6.10 eV) and electron affinity (2.44 eV) further reflected a dual capacity for controlled electron donation and acceptance, favoring charge–transfer interactions and electrostatic complementarity within the DNA microenvironment. Compared to more rigid analogues (*e.g.*, **9e**) or more reactive derivatives (*e.g.*, **9b**), **9f** presented an electronically optimized profile supporting reversible binding rather than excessive reactivity.

Global reactivity descriptors further reinforced this interpretation. The electronegativity (χ = 4.27 eV) and chemical hardness (η = 1.83 eV) place **9f** in an intermediate reactivity

Table 3 DFT analysis parameters of the newly synthesized *s*-triazine-isatin hybrid **8** and azole linked *s*-triazine-isatin hybrids **9a–f**

Compds	8	9a	9b	9c	9d	9e	9f
R_1, Azole	4-Br, Br	4-Br, benzo-thiazole	4-Br, benzoxazole	4-Br, oxadiazole	4-Br, tetrazole	H, tetrazole	4-Ph, tetrazole
E_{HOMO} (eV)	−6.21	−5.92	−5.69	−6.00	−6.15	−6.34	−6.10
E_{LUMO} (eV)	−2.51	−2.38	−2.25	−2.29	−2.47	−2.45	−2.44
Energy gap (ΔE_{Gap})	3.71	3.53	3.41	3.71	3.68	3.90	3.65
Ionization potential IP (eV)	6.21	5.92	5.69	6.00	6.15	6.34	6.10
Electron affinity EA (eV)	2.51	2.38	2.25	2.29	2.47	2.45	2.44
Electronegativity χ (eV)	4.36	4.15	3.97	4.14	4.31	4.40	4.27
Electrochemical potential μ (eV)	−4.36	−4.15	−3.97	−4.14	−4.31	−4.40	−4.27
Hardness η (eV)	1.85	1.77	1.72	1.86	1.84	1.95	1.83
Softness S (eV)	0.54	0.57	0.58	0.54	0.54	0.51	0.55
Electrophilicity ω (eV)	5.13	4.87	4.68	4.53	5.05	4.96	4.98

regime, while its softness ($S = 0.55$ eV^{-1}) indicated adequate polarizability to adapt to the nanoscale curvature of DNA grooves. The electrophilicity index ($\omega = 4.98$ eV) suggested moderate electrophilic character conducive to stable, non-covalent association. Importantly, the extended π-conjugation introduced by the phenyl-tetrazole substituent enhanced electron delocalization and aromatic surface area, potentially strengthening van der Waals and π–π interactions within AT-rich regions. Collectively, these electronic parameters provided a mechanistic rationale for the enhanced binding affinity observed for **9f**, supporting its role as a structurally and electronically favorable DNA-recognition scaffold within the synthesized series.

As illustrated in Fig. 7, the LUMO orbitals of the most potent compound **9f** are predominantly localized over the π-system of the *s*-triazine core, while the HOMO orbitals are primarily distributed across the phenyl ring and azole moiety. This spatial separation of electron density highlighted the key structural regions implicated in potential biological interactions. The visual representation provided in Fig. 7 further explained the distinct areas of electron localization within the molecule.

The observed HOMO → LUMO transition suggested a notable charge transfer interaction from the peripheral substituents toward the electron-deficient triazine ring, which may significantly contribute to the compound's reactivity and binding behavior. This intramolecular electron delocalization enhanced the electronic communication between molecular fragments and is likely to influence the compound's biological activity. Such charge transfer dynamics, coupled with favorable electronic properties, render compound **9f** a promising candidate for further pharmacological exploration.

In addition, the molecular electrostatic potential (MEP) analysis offered comprehensive insights into the electrostatic surface characteristics of compound **9f**, which feature a 4-phenyl substitution on the phenoxy ring. The MEP map (Fig. 7) revealed the most negative electrostatic potential region at -6.628×10^{-2} and the most positive at $+6.628 \times 10^{-2}$, effectively outlining the regions of electron-rich and electron-deficient character. The color scale employed in the MEP map follows the gradient: blue > green > yellow > orange > red, where blue corresponds to the most electron-attracting (electronegative) zones, and red signifies the most electron-repelling (electropositive) areas.

Notably, nucleophilic regions in compound **9f**, predominantly centered on the nitrogen atoms of the *s*-triazine and tetrazole moieties are visualized as deep blue zones, indicating strong electron density and potential for electrophilic attack. Conversely, electrophilic regions are largely associated with oxygen atoms and aromatic phenyl rings, which appear in deep

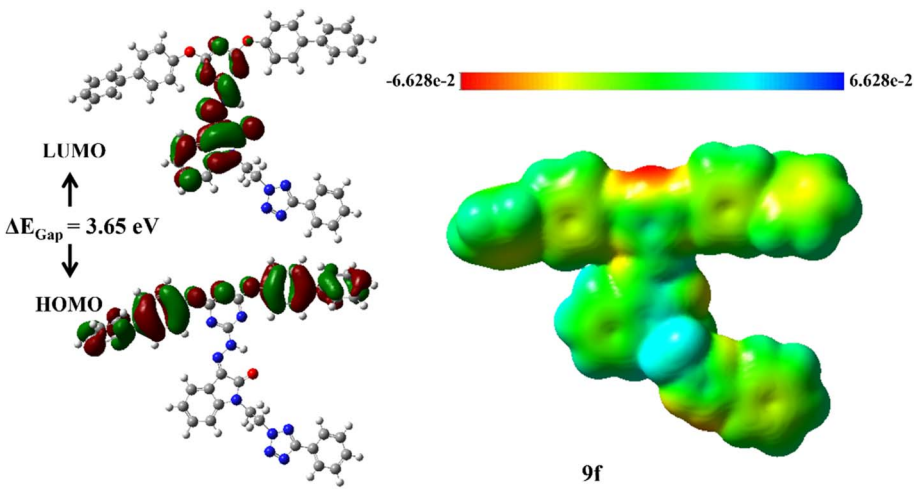

Fig. 7 HOMO, LUMO and 3D-MEP of compound **9f**.

Table 4 *In silico* pharmacokinetic parameters of compounds **8** & **9a–f** estimated through SwissADME and pkCSM web servers

Compound	Log P^a	TPSA^b (Å^2)	Caco-2 perm^c	Int. abs^d	VDss^e	AMES toxicity^f
8	5.55	101.83	0.601	100	−0.345	No
9a	7.13	168.26	0.722	100	−0.419	No
9b	6.58	153.16	0.641	100	−0.525	No
9c	7.00	166.05	0.412	100	−0.461	No
9d	5.51	145.43	0.089	100	−0.548	No
9e	4.34	145.43	0.16	100	−0.692	No
9f	6.84	145.43	−0.277	100	−0.265	No
CBZ	4.40	98.78	0.166	100	−1.023	No

[a] log of octanol–water partition coefficient (SwissADME[69]). [b] Topological Polar Surface Area (TPSA) (SwissADME[69]). [c] Caco-2 cell permeability as estimation of absorption at human intestinal mucosa[70] (pkCSM prediction[71]). [d] Proportion (%) of compound absorbed through the human small intestine[70] (pkCSM prediction[71]). [e] Steady-state volume of distribution (VDss) (pkCSM prediction[71]). [f] AMES toxicity (pkCSM prediction[71]).

yellow to red tones, suggesting areas prone to nucleophilic interactions. This detailed MEP visualization, as presented in Fig. 7, enabled the identification of potential reactive sites and supported the proposed bioactive nature of compound **9f**.

Collectively, these computational findings highlight the influence of azole and substituent variations on the electronic characteristics of *s*-triazine-isatin hybrids. The modulation of HOMO–LUMO energies, electronegativity, and electrophilicity suggested these compounds possess tunable properties suitable for further exploration in structure–activity relationship (SAR) studies and potential interaction with biomolecular targets.

2.6 *In silico* ADMET analyses

To assess the pharmacokinetic and toxicological suitability of the newly synthesized *s*-triazine-isatin hybrid **8** and azole linked *s*-triazine-isatin hybrids **9a–f**, a comprehensive *in silico* ADMET analysis was conducted (Table 4). The dataset included compound **8**, without azole motif, and compounds **9a–9f**, which were structurally diversified through the incorporation of different heterocyclic motifs at the triazine-isatin periphery. Specifically, **9a** features a benzothiazole ring, **9b** a benzoxazole, **9c** an oxadiazole, and **9d–9f** share a tetrazole moiety. Variation in the R_1 substitution was also introduced: **9a–9d** possess a 4-bromophenoxy group, **9e** a simple phenoxy group, and **9f** a bulkier 4-phenylphenoxy group.

Compound **9f** (R_1 = 4-phenyl, azole = tetrazole) emerged as a promising candidate in the series, exhibiting a favorable balance of pharmacokinetic and DNA-binding properties. It showed full predicted intestinal absorption (100%) and moderate tissue distribution (VDss = −0.265), with a log P of 6.84 and TPSA of 145.43 Å^2. Although its predicted Caco-2 permeability (−0.277) was lower than some analogs, it remains within an acceptable range for oral bioavailability. Importantly, **9f** displayed no predicted AMES toxicity. Moreover, ADMET trends indicate that moderate lipophilicity (log P 5–7) combined with sufficient TPSA (≈145–168 Å^2) supports good intestinal absorption and manageable tissue distribution, while avoiding genotoxicity across the series **9a–f**.

Overall, **9f** represents a balanced profile, combining strong DNA affinity, favorable pharmacokinetics, and low toxicity, highlighting its potential as a lead compound for further optimization. Other derivatives showed variable binding and absorption, largely influenced by azole type and substituent electronics, consistent with the observed SAR patterns.

Furthermore, toxicity predictions for compound **9f** have shown that it falls within GHS class V, with an LD_{50} of 3500 mg kg^{-1}, indicating that it may be harmful if swallowed but overall suggests moderate safety.[72] Moreover, StopTox results further confirmed that **9f** has been non-toxic in inhalation, dermal, skin irritation, corrosion, and sensitization assessments.[73]

The convergence of spectroscopic and computational data supports a coherent mechanistic model for DNA recognition by the azole-linked *s*-triazine-isatin hybrids. The observed hypochromic shifts in the UV-vis spectra, in the absence of pronounced bathochromic displacement, indicate a non-intercalative binding mode consistent with minor groove association. The experimentally determined binding constants (10^3–10^5 M^{-1}) fall within the range reported for classical groove-binding chemotypes, suggesting moderate yet specific affinity under physiological conditions. Thermodynamic analysis indicates spontaneous complex formation, with enthalpic contributions likely arising from dispersive and hydrogen-bonding interactions. Among the series, compound **9f** displayed the most favorable binding profile, reflecting an optimal balance between aromatic surface complementarity and heteroatom-directed interactions within AT-rich regions of the groove.

Computational modeling substantiates these experimental observations at atomic resolution. Docking studies revealed preferential localization of **9f** within the DNA minor groove, while molecular dynamics simulations confirmed the persistence of this binding orientation without inducing global helix distortion. MM/GBSA decomposition identified van der Waals forces as the dominant stabilizing contribution, accompanied by supportive electrostatic interactions and an opposing polar solvation penalty—an energetic signature characteristic of groove-binding ligands. Principal component and free energy landscape analyses further demonstrated ligand-induced restriction of DNA conformational sampling, indicating stabilization of specific conformational substates rather than large-scale structural perturbation. The strong agreement between spectroscopic behavior, docking orientation, and dynamic stability underscores a groove-directed recognition mechanism governed by nanoscale shape complementarity and hydrophobic packing. Collectively, these findings position the azole-linked *s*-triazine-isatin scaffold

as a structurally tunable platform for rational development of selective DNA-interactive agents.

3. Conclusions

This study establishes azole-linked *s*-triazine-isatin hybrids as structurally tunable nanoscale scaffolds capable of selective groove recognition, offering a foundation for the rational design of DNA-targeted therapeutics. A series of azole-linked *s*-triazine-isatin hybrids **9a–f** were successfully synthesized and systematically evaluated for their DNA-binding properties through a combined experimental and computational approach. Spectroscopic investigations revealed moderate to strong binding affinities toward DNA, with binding constants in the range of 10^3–10^5 M^{-1}, indicating effective interaction between the synthesized ligands and the DNA helix.

Among the investigated compounds, derivative **9f** demonstrated the most favorable binding behavior, supported by both experimental and computational analyses. Molecular docking studies indicated that the compounds preferentially interact within the minor groove of DNA, forming stabilizing hydrogen bonding and hydrophobic interactions with nucleotide bases. These findings were further supported by molecular dynamics simulations, which confirmed the structural stability of the ligand–DNA complex and revealed consistent interaction patterns throughout the simulation trajectory. The enhanced binding affinity observed for tetrazole-containing derivatives may be attributed to their electron-rich heterocyclic framework and increased hydrogen-bonding capability, which promote stronger interactions with nucleic acid structures. Comparative analysis with previously reported DNA-binding small molecules suggests that the synthesized compounds exhibit binding characteristics typical of groove-binding ligands rather than classical intercalators.

Overall, the present study demonstrates that the integration of heterocyclic scaffolds with favorable electronic properties can lead to promising DNA-binding agents. The combined experimental and computational strategy provides valuable insights into the molecular determinants governing ligand–DNA recognition. These findings may contribute to the future design of potential DNA-targeting therapeutic agents, and further investigations involving extended simulations and biological evaluations are warranted to explore their pharmacological potential.

4 Experimental

4.1 Computational details

4.1.1 Density functional theory (DFT) calculations. All molecular structures were geometry-optimized using the Gaussian 09 Package.[74] The optimization was carried out employing the B3LYP functional with 3-21G basis set under standard conditions. Frequency calculations confirmed that all optimized structures correspond to true minima on the potential energy surface. Frontier molecular orbitals (HOMO and LUMO) and associated global reactivity descriptors and molecular electrostatic potential (MEP) were computed using GaussView 6.

4.1.2 Molecular docking studies. Molecular docking simulations were performed using Autodock Vina 1.5.7 (ref. 75) to evaluate the binding affinity of synthesized compounds with DNA (PDB ID: 3EY0) and human topoisomerase II (PDB ID: 3QX3). Prior to docking, all receptor structures were prepared by removing water molecules and co-crystallized ligands, followed by the addition of polar hydrogens and assignment of appropriate charges. Ligand structures were energy-minimized prior to docking. Grid box dimensions for the DNA target (3EY0) was set to ($80 \times 60 \times 60$), and grid center coordinates were (16.394, 10.415, 90.220) and the exhaustiveness value was 4. The docking protocol was validated by redocking of cocrystallized ligand in 3EY0 and RMSD was found to be <2 Å. The resulting docking poses were ranked based on binding affinity (kcal mol^{-1}), and the best conformations were selected for interaction analysis. Visualization and analysis of intermolecular interactions, including hydrogen bonding, π–π stacking, and hydrophobic contacts, were performed using Discovery Studio Visualizer[76] and PyMOL.[77]

4.1.3 Molecular dynamics (MD) simulations. MD simulations were performed using GROMACS 2021.5 and cloud computing resources to evaluate the stability and dynamic behavior of ligand–DNA and ligand–protein complexes.[18,74] The systems were constructed by placing each complex in a cubic simulation box with a minimum distance of 10 Å from the edges and solvated using the TIP3P explicit water model. Counter ions (Na^+/Cl^-) were added to neutralize the systems and reproduce physiological ionic strength. The AMBER99SB force field was employed for protein simulations, while compatible AMBER parameters were applied for DNA, and ligand parameters were generated using the GAFF2 force field *via* ACPYPE. Although OL15 is optimized for nucleic acids, AMBER99SB was selected due to its validated performance in mixed protein–ligand systems and compatibility with GAFF2 ligand parametrization. This ensures consistency across DNA–ligand and protein–ligand simulations.

Energy minimization was carried out using the steepest descent algorithm, followed by equilibration under NVT and NPT ensembles. The temperature was maintained at 300 K using the V-rescale thermostat, while pressure was controlled at 1 bar using the Parrinello–Rahman barostat. Production simulations were conducted with a time step of 2 fs, applying periodic boundary conditions in all directions. Long-range electrostatic interactions were treated using the Particle Mesh Ewald (PME) method with a cutoff distance of 1.0 nm. The total simulation times were 4 ns for DNA–ligand complexes and 10 ns for protein–ligand systems.

Trajectory analyses were performed to assess system stability and conformational dynamics, including root mean square deviation (RMSD), root mean square fluctuation (RMSF), radius of gyration (R_g), hydrogen bonding analysis, and principal component analysis (PCA). Binding free energies were further estimated using MM/GBSA and MM-PBSA methods to evaluate interaction stability throughout the simulations.

4.2 DNA interaction study by UV-visible spectroscopy

Salmon sperm DNA (SS-DNA) was dissolved in distilled water and stirred for 24 hours. The stock solution of SS-DNA provided

a ratio of UV absorbance at 260 and 280 nm (A_{260}/A_{280}) of 1.89, indicating that the DNA was sufficiently free of proteins. The bulk DNA solution was further diluted to 10 folds to show maximum absorbance at 260 nm. The concentration of DNA stock solution was measured using molar absorptivity coefficient (ε) value of 6600 $M^{-1}cm^{-1}$ at 260 nm.[78] Solutions of compounds (50 μM) were prepared in DMSO and UV-vis absorption spectra of the compounds were recorded in the absence of DNA. The experiments were repeated with the same concentration of compounds and varying the concentration of DNA solutions (5–35 μM). UV-vis absorption spectra were recorded on Shimadzu 1700 UV-visible spectrophotometer.

4.3 Synthesis of *s*-triazine-isatin hybrid (8)

To the solution of 1-(2-bromoethyl) isatin **5** (0.25 mmol, 1.0 eq.) in ethanol, glacial acetic acid (few drops) was added followed by the addition of 4-bromophenoxy-linked hydrazinyl *s*-triazine **3** (0.25 mmol, 1.0 eq.). The reaction progress was monitored at regular intervals using thin-layer chromatography. *s*-Triazine-isatin hybrid **8** was precipitated out from the reaction mixture after 3–4 hours of reflux, which was subsequently filtered, dried, and recrystallized from ethanol to yield the pure product.

Yellow solid; yield: 79%; melting point: 246–248 °C; R_f: 0.40 ($CHCl_3$: MeOH, 9 : 1); FT-IR $\bar{\nu}$ (cm^{-1}): 1148 (C–N stretch; lactam), 1205 (C_{sp2}–O stretch; ether), 1343 (C_{sp3}–H bend; methylene), 1482, 1549 (C=C stretch; aromatic), 1619 (C=N stretch; imine), 1690, (C=O stretch; amide), 2980 (C_{sp3}–H stretch), 3097 (C_{sp2}–H stretch), 3187 (N–H stretch); ^{1}H NMR (300 MHz, DMSO-d_6) δ (ppm): 12.86 (s, 1H, –NH), 7.68–6.92 (m, 12H, Ar–H), 4.19 (t, 2H, ^3J = 6 Hz, –CH_2), 3.74 (t, 2H, ^3J = 6 Hz, –CH_2); ^{13}C NMR (75 MHz, DMSO-d_6) δ (ppm): 167.1, 161.5, 151.1, 142.7, 132.8, 124.6, 124.4, 120.9, 119.4, 118.7, 41.4, 29.8.

4.4 Synthesis of azole linked *s*-triazine-isatin hybrids (9a–f)

A solution of respective isatins **7a–d** (0.25 mmol, 1.0 eq.) in ethanol was prepared, to which a few drops of glacial acetic acid were added. Subsequently, phenoxy-linked hydrazinyl-*s*-triazines 3 (0.25 mmol, 1.0 eq.) were introduced into the reaction mixture. The mixture was refluxed, and the progress of the reaction was monitored at regular intervals by thin-layer chromatography (TLC). After 3–4 hours of reflux, the corresponding triazine-based hydrazone derivatives**9a–f** precipitated from the reaction mixture. The solid products were collected by filtration, dried, and recrystallized from ethanol to afford the pure compounds.

4.4.1. 1-(2-(Benzo[*d*]thiazol-2-ylthio)ethyl)-3-(2-(4,6-bis(4-bromophenoxy)-1,3,5-triazin-2-yl)hydrazineylidene)indolin-2-one (9a). Yellow solid; yield: 82%; melting point: 231–233 °C; R_f: 0.42 ($CHCl_3$, MeOH, 9 : 1); FT-IR $\bar{\nu}$ (cm^{-1}): 1148 (C–N stretch; lactam), 1281 (C_{sp2}–O stretch; ether), 1345 (C_{sp3}–H bend; methylene), 1482, 1560 (C=C stretch; aromatic), 1619 (C=N stretch; imine), 1769 (C=O stretch; amide), 2980 (C_{sp3}–H stretch), 3067 (C_{sp2}–H stretch), 3271 (N–H stretch); ^{1}H NMR (300 MHz, DMSO-d_6) δ (ppm): 12.74 (s, 1H, –NH), 8.02–7.13 (m, 16H, Ar–H), 4.20 (t, 2H, ^3J = 6 Hz, –CH_2), 3.69 (t, 2H, ^3J = 6 Hz, –CH_2); ^{13}C NMR (75 MHz, DMSO-d_6) δ (ppm): 167.3, 166.3, 164.4, 159.8, 156.2, 151.2, 149.7, 143.2, 136.2, 135.2, 132.8, 126.9, 125.0, 124.4, 121.4, 118.9, 116.5, 113.4, 110.8, 43.0, 33.9.

4.4.2. 1-(2-(Benzo[*d*]oxazol-2-ylthio)ethyl)-3-(2-(4,6-bis(4-bromophenoxy)-1,3,5-triazin-2-yl)hydrazineylidene)indolin-2-one (9b). Yellow solid; yield: 78%; melting point: 221–223 °C; R_f: 0.39 ($CHCl_3$, MeOH, 9 : 1); FT-IR $\bar{\nu}$ (cm^{-1}): 1146 (C–N stretch; lactam), 1282 (C_{sp2}–O stretch; ether), 1340 (C_{sp3}–H bend; methylene), 1480, 1550 (C=C stretch; aromatic), 1610 (C=N stretch; imine), 1765 (C=O stretch; amide), 2980 (C_{sp3}–H stretch), 3067 (C_{sp2}–H stretch), 3270 (N–H stretch);^{1}H NMR (300 MHz, DMSO-d_6) δ (ppm): 12.70 (s, 1H, –NH), 7.69–7.11 (m, 16H, Ar–H), 4.22 (t, 2H,^3J = 6 Hz, –CH_2), 3.61 (t, 2H, ^3J = 6 Hz, –CH_2); ^{13}C NMR (75 MHz, DMSO-d_6) δ (ppm): 167.1, 164.2, 161.7, 161.6, 151.7, 151.2, 142.9, 141.5, 136.0, 132.8, 125.1, 124.7, 124.4, 123.7, 120.9, 119.4, 118.7, 110.5, 56.4, 29.7.

4.4.3. 3-(2-(4,6-Bis(4-bromophenoxy)-1,3,5-triazin-2-yl) hydrazineylidene)-1-(2-((5-(4-chlorophenyl)-1,3,4-oxadiazol-2-yl) thio)ethyl)indolin-2-one (9c). Yellow solid; yield: 79%; melting point: 246–248 °C; R_f: 0.40 ($CHCl_3$, MeOH, 9 : 1); FT-IR $\bar{\nu}$ (cm^{-1}): 1140 (C–N stretch; lactam), 1278 (C_{sp2}–O stretch; ether), 1335 (C_{sp3}–H bend; methylene), 1470, 1550 (C=C stretch; aromatic), 1610 (C=N stretch; imine), 1760 (C=O stretch; amide), 2981 (C_{sp3}–H stretch), 3060 (C_{sp2}–H stretch), 3275 (N–H stretch); ^{1}H NMR (300 MHz, DMSO-d_6) δ (ppm): 12.65 (s, 1H, –NH), 7.96–7.08 (m, 16H, Ar–H), 4.21 (t, 2H, ^3J = 6 Hz, –CH_2), 3.62 (t, 2H, ^3J = 6 Hz, –CH_2); ^{13}C NMR (75 MHz, DMSO-d_6) δ (ppm): 167.0, 164.7, 161.6, 153.1, 151.2, 144.2, 141.9, 137.2, 132.8, 129.9, 128.5, 124.4, 122.5, 118.6, 112.6, 110.6, 49.4, 36.2.

4.4.4. 3-(2-(4,6-Bis(4-bromophenoxy)-1,3,5-triazin-2-yl) hydrazineylidene)-1-(2-(5-phenyl-2*H*-tetrazol-2-yl)ethyl)indolin-2-one (9d). Yellow solid, yield: 78%; melting point: 209–210 °C[294]; R_f: 0.46 (*n*-hexane: ethyl acetate, 3 : 2); FT-IR $\bar{\nu}$ (cm^{-1}): 1192 (C–N stretch; lactam), 1205 (C_{sp2}–O stretch; ether), 1346 (C_{sp3}–H bend; methylene), 1492, 1571 (C=C stretch; aromatic), 1619 (C=N stretch; imine), 1709, (C=O stretch; amide), 2935 (C_{sp3}–H stretch), 3058 (C_{sp2}–H stretch), 3229 (N–H stretch); ^{1}H NMR (300 MHz, $CDCl_3$) δ (ppm):12.71 (s, 1H, –NH), 8.03–6.60 (m, 17H, Ar–H), 5.02 (t, 2H, ^3J = 8 Hz, –CH_2), 4.38 (t, 2H, ^3J = 8 Hz, –CH_2), ^{13}C NMR; (75 MHz, DMSO-d_6) δ (ppm): 167.4, 165.7, 161.6, 150.1, 141.8, 135.1, 132.6, 131.3, 130.5, 129.5, 128.9, 126.9, 123.9, 122.9, 122.2, 119.5, 119.2, 108.2, 50.2, 39.4.

4.4.5. 3-(2-(4,6-Diphenoxy-1,3,5-triazin-2-yl)hydrazineylidene)-1-(2-(5-phenyl-2*H*-tetrazol-2-yl)ethyl)indolin-2-one (9e). Yellow solid; yield: 84%; melting point: 236–238 °C[294]; R_f: 0.35 (*n*-hexane: ethyl acetate, 3 : 2); FT-IR $\bar{\nu}$ (cm^{-1}): 1148 (C–N stretch; lactam), 1205 (C_{sp2}–O stretch; ether), 1343 (C_{sp3}–H bend; methylene), 1482, 1549 (C=C stretch; aromatic), 1619 (C=N stretch; imine), 1690, (C=O stretch; amide), 2980 (C_{sp3}–H stretch), 3097 (C_{sp2}–H stretch), 3187 (N–H stretch); ^{1}H NMR (300 MHz, $CDCl_3$) δ (ppm):12.71 (s, 1H, –NH), 8.03–6.60 (m, 19H, Ar–H), 5.02 (t, 2H, ^3J = 8 Hz, –CH_2), 4.38 (t, 2H, ^3J = 8 Hz, –CH_2); ^{13}C NMR; (75 MHz, DMSO-d_6) δ (ppm): 167.3, 165.6, 161.5, 141.7, 135.1, 132.5, 131.4, 130.5, 128.9, 126.8, 123.8, 123.3, 122.2, 119.4, 119.2, 108.2, 50.2, 39.4.

4.4.6. 3-(2-(4,6-Bis([1,1′-biphenyl]-4-yloxy)-1,3,5-triazin-2-yl) hydrazineylidene)-1-(2-(5-phenyl-2*H*-tetrazol-2-yl)ethyl)indolin-2-one (9f). Yellow solid; yield: 78%; melting point: 209–210 °

C^{294}; R_f: 0.46 (*n*-hexane: ethyl acetate, 3 : 2); FT-IR $\bar{\nu}$ (cm^{-1}): 1148 (C–N stretch; lactam), 1205 (C_{sp2}–O stretch; ether), 1343 (C_{sp3}–H bend; methylene), 1482, 1549 (C=C stretch; aromatic), 1619 (C=N stretch; imine), 1690, (C=O stretch; amide), 2980 (C_{sp3}–H stretch), 3097 (C_{sp2}–H stretch), 3187 (N–H stretch); ^{1}H NMR (300 MHz, $CDCl_3$) δ (ppm):12.67 (s, 1H, –NH), 8.03–6.59 (m, 27H, Ar–H), 5.01 (t, 2H, $^3J = 8$ Hz, $-CH_2$), 4.38 (t, 2H, $^3J = 8$ Hz, $-CH_2$); ^{13}C NMR; (75 MHz, DMSO-d_6) δ (ppm): 167.4, 165.6, 161.5, 141.7, 135.1, 131.9, 131.4, 130.5, 129.5, 129.4, 128.9, 126.8, 126.1, 125.9, 123.8, 123.3, 122.1, 121.5, 121.4, 108.1, 50.2, 39.1.

Conflicts of interest

The authors report no conflicts of interest.

Data availability

The data supporting the findings of this study are available within the article and its supplementary information (SI). Supplementary information: experimental procedures, spectroscopic data, computational details, molecular docking, molecular dynamics simulation results, and density functional theory (DFT) calculations. See DOI: https://doi.org/10.1039/d5na01140j.

Acknowledgements

Higher Education Commission (HEC) of Pakistan and The World Academy of Sciences (TWAS) are gratefully acknowledged for projects, 9225/Federal/NRPU/R&D/HEC/2017 and 13–419 RG/PHA/AS_CUNESCO FR: 3240279216, respectively.

References

1 B. Liu, H. Zhou, L. Tan, K. T. H. Siu and X.-Y. Guan, *Signal Transduct. Targeted Ther.*, 2024, **9**, 175.
2 C. Zhao, W. Song, J. Wang, X. Tang and Z. Jiang, *Chem. Commun.*, 2025, **61**, 1962–1977.
3 A. Mushtaq, P. Wu and M. M. Naseer, *Pharmacol. Ther.*, 2024, **254**, 108579.
4 N. K. Sharma, A. Bahot, G. Sekar, M. Bansode, K. Khunteta, P. V. Sonar, A. Hebale, V. Salokhe and B. K. Sinha, *Cancers*, 2024, **16**, 680.
5 S. Zheng, R. Chen, L. Zhang, L. Tan, L. Li, F. Long and T. Wang, *Eur. J. Med. Chem.*, 2024, 116702.
6 D. Li, X. Peng, Z. Hu, S. Li, J. Chen and W. Pan, *Eur. J. Med. Chem.*, 2024, **264**, 115982.
7 A. Rismanbaf, *Cancer Rep.*, 2024, **7**, e1945.
8 A. M. Abu-Dief, T. El-Dabea, R. M. El-Khatib, M. Feizi-Dehnayebi, F. S. Aljohani, K. Al-Ghamdi, I. O. Barnawi and M. A. E. A. A. Ali, *J. Mol. Liq.*, 2024, **399**, 124422.
9 I. El-Deen, A. Shoair and M. El-Bindary, *J. Mol. Liq.*, 2018, **249**, 533–545.
10 G. Magdy, F. Belal, A. F. A. Hakiem and A. M. Abdel-Megied, *Int. J. Biol. Macromol.*, 2021, **182**, 1852–1862.
11 R. Wing, H. Drew, T. Takano, C. Broka, S. Tanaka, K. Itakura and R. E. Dickerson, *Nature*, 1980, **287**, 755–758.
12 N. C. Seeman, *Mol. Biotechnol.*, 2007, **37**, 246–257.
13 P. Zhan, A. Peil, Q. Jiang, D. Wang, S. Mousavi, Q. Xiong, Q. Shen, Y. Shang, B. Ding, C. Lin, Y. Ke and N. Liu, *Chem. Rev.*, 2023, **123**, 3976–4050.
14 L. Strekowski and B. Wilson, *Mutat. Res. Fundam. Mol. Mech. Mutagen.*, 2007, **623**, 3–13.
15 I. Saha, M. Hossain and G. Suresh Kumar, *J. Phys. Chem. B*, 2010, **114**, 15278–15287.
16 M. Sirajuddin, S. Ali and A. Badshah, *J. Photochem. Photobiol. B Biol.*, 2013, **124**, 1–19.
17 A. Ganguly, S. Ghosh and N. Guchhait, *Phys. Chem. Chem. Phys.*, 2015, **17**, 483–492.
18 D. Domyati, E. M. M. Ali, M. A. Hussien, B. Davaasuren, M. Jaremko and M. M. El-Bendary, *BMC Chem.*, 2025, **19**, 102.
19 Ž. Skok, N. Zidar, D. Kikelj and J. Ilaš, *J. Med. Chem.*, 2020, **63**, 884–904.
20 F. Mueller-Planitz and D. Herschlag, *Nucleic Acids Res.*, 2007, **35**, 3764–3773.
21 F. Arjmand, S. Parveen, M. Afzal and M. Shahid, *J. Photochem. Photobiol. B Biol.*, 2012, **114**, 15–26.
22 J.-H. Shi, T.-T. Liu, M. Jiang, J. Chen and Q. Wang, *J. Photochem. Photobiol. B Biol.*, 2015, **147**, 47–55.
23 H. Li, X. Bu, J. Lu, C. Xu, X. Wang and X. Yang, *Spectrochim. Acta Mol. Biomol. Spectrosc.*, 2013, **107**, 227–234.
24 R. Bera, B. K. Sahoo, K. S. Ghosh and S. Dasgupta, *Int. J. Biol. Macromol.*, 2008, **42**, 14–21.
25 J.-H. Shi, J. Chen, J. Wang and Y.-Y. Zhu, *Spectrochim. Acta Mol. Biomol. Spectrosc.*, 2015, **136**, 443–450.
26 Y. Guo, Q. Yue and B. Gao, *Int. J. Biol. Macromol.*, 2011, **49**, 55–61.
27 N. Shakibapour, F. Dehghani Sani, S. Beigoli, H. Sadeghian and J. Chamani, *J. Biomol. Struct. Dyn.*, 2019, **37**, 359–371.
28 A. Mushtaq, U. Azam, S. Mehreen and M. M. Naseer, *Eur. J. Med. Chem.*, 2023, **249**, 115119.
29 M. Altamimi, S. A. Syed, B. Tuzun, M. R. Alhazani, O. Alnemer and A. Bari, *J. Enzym. Inhib. Med. Chem.*, 2024, **39**, 2288548.
30 N. S. Haiba, H. H. Khalil, M. A. Moniem, M. H. El-Wakil, A. A. Bekhit and S. N. Khattab, *Bioorg. Chem.*, 2019, **89**, 103013.
31 A. S. Diakité, C. N. t. M. Ambeu-Loko, A. D. Yapi, C. Logé, A. Kacou, S. Kra, B. Baratte, S. Bach, S. Ruchaud and D. Sissouma, *Int. J. Pharmaceut. Res. Allied Sci.*, 2024, **13**, 1–11.
32 T. Verma, M. Sinha and N. Bansal, *Anti-Cancer Agents Med. Chem.*, 2020, **20**, 4–28.
33 I. Shawish, A. Barakat, A. Aldalbahi, A. M. Malebari, M. S. Nafie, A. A. Bekhit, A. Albohy, A. Khan, Z. Ul-Haq and M. Haukka, *ACS Omega*, 2022, **7**, 24858–24870.
34 A. El-Faham, M. Farooq, Z. Almarhoon, R. Abd Alhameed, M. A. Wadaan, B. G. de la Torre and F. Albericio, *Bioorg. Chem.*, 2020, **94**, 103397.
35 Q. Dai, Q. Sun, X. Ouyang, J. Liu, L. Jin, A. Liu, B. He, T. Fan and Y. Jiang, *Molecules*, 2023, **28**, 4278.
36 K. Vine, L. Matesic, J. Locke, M. Ranson and D. Skropeta, *Anti-Cancer Agents Med. Chem.*, 2009, **9**, 397–414.

37 W. M. Eldehna, M. A. El Hassab, M. F. Abo-Ashour, T. Al-Warhi, M. M. Elaasser, N. A. Safwat, H. Suliman, M. F. Ahmed, S. T. Al-Rashood and H. A. Abdel-Aziz, *Bioorg. Chem.*, 2021, **110**, 104748.
38 D. A. Gideon, P. Annadurai, V. Nirusimhan, A. Parashar, J. James and V. V. Dhayabaran, in *Handbook of Oxidative Stress in Cancer: Therapeutic Aspects*, Springer, 2021, pp. 1–25.
39 K. Dhahagani, M. P. Kesavan, K. G. G. Vinoth, L. Ravi, G. Rajagopal and J. Rajesh, *Mater. Sci. Eng. C*, 2018, **90**, 119–130.
40 Y.-O. Teng, H.-Y. Zhao, J. Wang, H. Liu, M.-L. Gao, Y. Zhou, K.-L. Han, Z.-C. Fan, Y.-M. Zhang and H. Sun, *Eur. J. Med. Chem.*, 2016, **112**, 145–156.
41 C. N. S. S. P. Kumar, D. K. Parida, A. Santhoshi, A. K. Kota, B. Sridhar and V. J. Rao, *Medchemcomm*, 2011, **2**, 486–492.
42 J. Jiang, X. Tang, W. Dou, H. Zhang, W. Liu, C. Wang and J. Zheng, *J. Inorg. Biochem.*, 2010, **104**, 583–591.
43 S. Zehra, M. Shavez Khan, I. Ahmad and F. Arjmand, *J. Biomol. Struct. Dyn.*, 2019, **37**, 1863–1879.
44 A. Terenzi, M. Fanelli, G. Ambrosi, S. Amatori, V. Fusi, L. Giorgi, V. T. Liveri and G. Barone, *Dalton Trans.*, 2012, **41**, 4389–4395.
45 L.-P. Peng, S. Nagarajan, S. Rasheed and C.-H. Zhou, *Medchemcomm*, 2015, **6**, 222–229.
46 A. Kamal, K. S. Reddy, M. N. A. Khan, R. V. Shetti, M. J. Ramaiah, S. Pushpavalli, C. Srinivas, M. Pal-Bhadra, M. Chourasia and G. N. Sastry, *Bioorg. Med. Chem.*, 2010, **18**, 4747–4761.
47 M. Ulular, N. Sarı, F. Han, H. Öğütçü and E. Hasanoğlu Özkan, *Pharm. Chem. J.*, 2024, **57**, 1609–1620.
48 R. Sultana, A. Ali, M. Rana, I. Ahmad, M. Kamthan, H. T. A. Almuqdadi, R. Mehandi, M. Abid and Z. M. El-Bahy, *J. Mol. Struct.*, 2024, **1318**, 139350.
49 A. Husain, C. S. Devi and B. Anupama, *J. Mol. Struct.*, 2023, **1291**, 135963.
50 N. Vamsikrishna, M. P. Kumar, G. Ramesh, N. Ganji, S. Daravath and Shivaraj, *J. Chem. Sci.*, 2017, **129**, 609–622.
51 V. R. Solomon, C. Hu and H. Lee, *Bioorg. Med. Chem.*, 2009, **17**, 7585–7592.
52 E. p. Başaran, S. Köprü, S. Akkoç and B. i. Türkmenoğlu, *ACS Omega*, 2024, **9**, 26503–26518.
53 R. Raju, K. Chidambaram, B. Chandrasekaran, M. F. Bayan, T. K. Maity, A. M. Alkahtani and H. C. Chandramoorthy, *J. Saudi Chem. Soc.*, 2023, **27**, 101598.
54 W. M. Eldehna, A. Altoukhy, H. Mahrous and H. A. Abdel-Aziz, *Eur. J. Med. Chem.*, 2015, **90**, 684–694.
55 M. M. El-Naggar, D. S. A. Haneen, A. B. M. Mehany and M. T. Khalil, *Int. J. Biol. Macromol.*, 2020, **150**, 1323–1330.
56 A. Mushtaq, R. Asif, W. A. Humayun and M. M. Naseer, *RSC Adv.*, 2024, **14**, 14051–14067.
57 A. Mushtaq and M. M. Naseer, *RSC Adv.*, 2025, **15**, 8443–8455.
58 A. Mushtaq and M. M. Naseer, *J. Mol. Struct.*, 2025, **1322**, 140558.
59 A. Mushtaq and M. M. Naseer, *ChemistrySelect*, 2025, **10**, e01774.
60 T. Linder, M. Schnürch and M. D. Mihovilovic, *Monatsh. Chem.*, 2018, **149**, 1257–1284.
61 S. Federico, A. Ciancetta, N. Porta, S. Redenti, G. Pastorin, B. Cacciari, K. N. Klotz, S. Moro and G. Spalluto, *Eur. J. Med. Chem.*, 2016, **108**, 529–541.
62 Ö. Akgül, A. H. Tarikoğullari, F. A. Köse, P. B. Kirmizibayrak and M. V. Pabuççuoğlu, *Turk. J. Chem.*, 2013, **37**, 204–212.
63 L. Firoozpour, L. Gao, S. Moghimi, P. Pasalar, J. Davoodi, M.-W. Wang, Z. Rezaei, A. Dadgar, H. Yahyavi, M. Amanlou and A. Foroumadi, *J. Enzyme Inhib. Med. Chem.*, 2020, **35**, 1674–1684.
64 S. Luikham, A. Mavani, D. Sinha and J. Bhattacharyya, *J. Phys. Chem. B*, 2023, **127**, 4966–4978.
65 A. B. Dileepan, T. D. Prakash, A. G. Kumar, P. S. Rajam, V. V. Dhayabaran and R. Rajaram, *J. Photochem. Photobiol. B Biol.*, 2018, **183**, 191–200.
66 N. Arshad, M. I. Mir, F. Perveen, A. Javed, M. Javaid, A. Saeed, P. A. Channar, S. I. Farooqi, S. Alkahtani and J. Anwar, *Molecules*, 2022, **27**, 354.
67 M. Bashiri, A. Jarrahpour, S. M. Nabavizadeh, S. Karimian, B. Rastegari, E. Haddadi and E. Turos, *Med. Chem. Res.*, 2021, **30**, 258–284.
68 J. A. Lemkul, *J. Phys. Chem. B*, 2024, **128**, 9418–9435.
69 A. Daina, O. Michielin and V. Zoete, *Sci. Rep.*, 2017, **7**, 42717.
70 V. P. DE, T. Blundell and D. Ascher, *Prof. Contrib. Colorado Sch. Mine*, 2015, 5.
71 D. E. V. Pires, T. L. Blundell and D. B. Ascher, *J. Med. Chem.*, 2015, **58**, 4066–4072.
72 P. Banerjee, E. Kemmler, M. Dunkel and R. Preissner, *Nucleic Acids Res.*, 2024, **52**, W513–w520.
73 J. V. B. Borba, V. M. Alves, R. C. Braga, D. R. Korn, K. Overdahl, A. C. Silva, S. U. S. Hall, E. Overdahl, N. Kleinstreuer, J. Strickland, D. Allen, C. H. Andrade, E. N. Muratov and A. Tropsha, *Environ. Health Perspect.*, 2022, **130**, 27012.
74 A. Frisch, Wallingford, Usa, 25p, 2009, 470.
75 O. Trott and A. J. Olson, *J. Comput. Chem.*, 2010, **31**, 455–461.
76 Dassault Systèmes Biovia, *Discovery Studio Modeling Environment*, Biovia, San Diego, CA, USA, 2016.
77 W. L. DeLano, *CCP4 Newsl. Protein Crystallogr.*, 2002, **40**, 82–92.
78 H. Ullah, V. Previtali, H. B. Mihigo, B. Twamley, M. K. Rauf, F. Javed, A. Waseem, R. J. Baker and I. Rozas, *Eur. J. Med. Chem.*, 2019, **181**, 111544.